Nanoscale

PAPER

View Article Online
View Journal | View Issue

Cite this: *Nanoscale*, 2025, **17**, 25821

Ligand-induced room-temperature synthesis of NiCoSe nanostructures: a highly efficient electrocatalyst for hydrazine-assisted hydrogen production

Athma E. Praveen,[a] Viplove Mishra,[a] Aditi Chandrasekar*[b] and Venkataramanan Mahalingam *[a]

Transition metal selenides are considered to be promising electrode materials to catalyze various electrocatalytic reactions. The synthesis of these metal selenides involves harsh synthetic conditions and multistep routes. Herein, a room-temperature ligand-assisted strategy has been developed to synthesize NiSe, CoSe, and NiCoSe in a pure phase. This study delves into the significant impact of ligands on nanoparticle synthesis, with a particular focus on their pivotal role in finely adjusting the crystalline phase of the resulting nanomaterials. We have focused on identifying the specific ligands that can effectively manipulate nucleation and growth processes for the synthesis of specific crystal structures of MSe (M = Ni, Co). The role of functional groups in ligands was probed, and it was found that the carboxylic acid groups play a key role in facilitating the synthesis of pure-phase NiSe, CoSe, and NiCoSe. Through a detailed examination of the existing literature and theoretical calculations, we have investigated the mechanism and role of carboxylate ligands in MSe (M = Ni, Co) formation. Computational investigations suggest that the formation of a metastable metal–carboxylate intermediate complex optimizes the reaction condition, makes it more favorable for reorientation, and allows selenium to approach the nickel center. Furthermore, the synthesis of NiCoSe aims to enhance the electrocatalytic performance of NiSe and CoSe, as the bimetallic (NiCoSe) material exhibits superior electrochemical properties compared to its monometallic counterparts. The electrocatalytic activities of the synthesized transition metal selenides were evaluated for hydrazine-assisted water splitting. Bimetallic NiCoSe displays superior electrocatalytic performance toward hydrazine oxidation and hydrogen evolution reactions compared to the monometallic phases of NiSe and CoSe. The bimetallic component requires a potential of 0.20 V *vs.* RHE and an overpotential of 0.20 V to attain 10 mA cm^{-2} for the HzOR and HER, respectively. Moreover, NiCoSe displays excellent activity as a bifunctional catalyst, and it requires a very low cell voltage of 0.45 V to attain a current density of 10 mA cm^{-2} for H_2 production. The free energy profile of the stepwise HzOR has been investigated in detail. The computational results reveal the enhanced feasibility of the HzOR on NiCoSe (1 : 1) compared to NiSe. Therefore, briefly, this work offers an innovative synthesis protocol for the ligand-induced room-temperature synthesis of transition metal selenide nanostructures and their application for hydrazine-assisted hydrogen production.

Received 22nd June 2025,
Accepted 8th October 2025

DOI: 10.1039/d5nr02653a

rsc.li/nanoscale

1. Introduction

Hybrid water splitting is emerging as one of the potential strategies for energy-efficient hydrogen production.[1–6] Among hybrid water splitting systems, coupling of the hydrogen evolution reaction (HER) with the hydrazine oxidation reaction (HzOR) is considered to be one of the most effective strategies for energy-efficient hydrogen production.[3,7–9] Hydrazine oxidation-assisted hydrogen production systems provide a variety of advantages over traditional OER-assisted water-splitting systems, for instance, the reduction in the overall energy requirement of an electrolyzer, release of nontoxic and stable N_2 as a byproduct, elimination of the risk of gas crossover explosion, and the feasibility of making a membrane-free electrochemical cell system.[7,10–12,13] To explore the application of hydrazine oxidation-assisted hydrogen production, an

[a]*Department of Chemical Sciences, Indian Institute of Science Education and Research (IISER) Kolkata, Mohanpur, 741246 West Bengal, India.*
E-mail: mvenkataramanan@yahoo.com
[b]*School of Arts and Sciences, Azim Premji University, Bangalore 562125, India.*
E-mail: Aditi.chandrasekar@apu.edu.in

efficient bifunctional electrocatalyst is required for the HzOR and HER.[7,10–12] Recently, nanomaterial synthesis has been a cornerstone of modern materials science and engineering, with applications spanning catalysis, sensing, energy storage, and biomedical imaging. The precise manipulation of the crystalline phase of nanoparticles is important, as it substantially affects their physical and chemical properties. Understanding and controlling the specific crystalline phase of materials allow researchers to tailor their surface reactivity, catalytic activity, and durability, ultimately advancing electrocatalytic performance for specific applications, such as water splitting, fuel cells, and electrochemical sensing.[14] Lately, various transition metal-based electrocatalysts have been explored for electrocatalysis applications.[15–22] Among transition metal-based electrocatalysts, transition metal chalcogenides have been proven as promising electrode materials for hydrazine oxidation-assisted hydrogen production.[23–30] Specially, Ni and Co selenides, such as NiSe, CoSe, $NiSe_2$, and $CoSe_2$, have been reported to electrocatalyze the HER, OER, and HzOR. However, these materials have been synthesized *via* electrodeposition, hydrothermal or solvothermal treatment, microwave irradiation, and thermal injection methods, which require high temperatures and long reaction times.[31,32] This demands the development of facile and efficient synthesis routes that are applicable on a large scale.

In recent years, considerable attention has been devoted to understanding the role of ligands in governing nanoparticle phase control.[33] Ligands play a crucial role in the nucleation and growth processes owing to their ability to influence nucleation kinetics by acting as either stabilizers or inhibitors, and they can exert control over the subsequent growth of nanoparticles by modifying surface interactions. The interactions between ligands and the nanoparticle surface have a profound impact on the resulting crystal structure and, consequently, the physical and chemical properties of the nanocrystals produced. Ligands can selectively bind to specific facets or crystallographic planes of the growing nanoparticles, thereby modifying the surface energy and surface chemistry. In this manner, they serve as stabilizing agents, lowering the energy barrier for nucleation, or as kinetic inhibitors, impeding the formation of nuclei and subsequently affecting the growth of nanoparticles.[33] By carefully selecting appropriate ligands, researchers tailor the synthesis conditions to achieve the desired nanoparticle properties such as size, shape, and surface functionality.[34,35] For example, Revaprasadu *et al.* synthesized various metal chalcogenides and phosphides by tuning different ligands, surfactants, and synthetic conditions.[36] Our group has reported how the use of thiol-based ligands leads to the selective synthesis and stabilization of the Ni_2P phase, while thiol-free ligands transform the Ni_2P phase into the $Ni_{12}P_5$ phase of nickel phosphide.[37] Similarly, Pramanik *et al.* synthesized the NiTe phase using tartaric acid as a ligand.[38] Generally, these syntheses involve multiple steps and harsh synthetic conditions. In addition, the exact mechanism explaining why the use of particular ligands leads to the formation of selective phases has not been explored.

Herein, a ligand-mediated room-temperature synthesis route is reported for the preparation of NiSe and CoSe in the pure phase. The synthesis involves carboxylic acid-based ligands and elemental Se as a selenide source to facilitate the synthesis of pure-phase NiSe and CoSe. The role of functional groups in ligands is probed by synthesizing NiSe materials using ligands with different functional groups. We have found that the presence of dicarboxylic acid groups in the ligand plays a key role in the synthesis of nickel and cobalt selenides. The precise coordination between ligands and the nanoparticle surface is not fully known due to limited access to the surface structure at the nanoscale. However, our study sheds light on the importance of ligand-surface interactions in controlling the crystal structure of nanocrystals. Understanding these interactions is crucial for synthesizing nanocrystals with the desired properties and gaining insights into crystallization processes in general. In addition, it is known that bimetallic materials often show superior electrochemical performance to monometallic materials due to the synergistic effect of the two metal sites. Therefore, NiCoSe materials with different Ni : Co ratios are synthesized to further boost the electrocatalytic performance. The as-synthesized transition metal selenide catalysts are evaluated for hydrazine-assisted water splitting. Bimetallic NiCoSe displays superior electrocatalytic performance to pure-phase NiSe and CoSe. NiCoSe shows excellent activity toward hydrazine oxidation and requires a potential of 0.20 V *vs.* RHE to attain 10 mA cm^{-2}. To achieve a high current density of 300 mA cm^{-2}, it needs a potential of only 700 mV without the assistance of electrochemically active substrates such as Ni foam or Co foam. Moreover, NiCoSe displays excellent activity as a bifunctional catalyst by requiring a very low cell voltage of 0.45 V to attain a current density of 10 mA cm^{-2} for H_2 production.

2. Experimental section

2.1 Synthesis of MSe (M = Ni, Co)

Metal selenides were synthesized using ligands at room temperature. Briefly, 2 mmol MCl_2 (M = Ni, Co) and tartaric acid (*vide infra*) were dissolved in 20 mL of deionized water. A clear solution of 3 mmol Se and 2 mmol $NaBH_4$ was prepared by stirring for 45 min under mild heating conditions. Subsequently, the as-prepared metal solution was added to the Se solution. Immediately, a black precipitate was formed and was kept under constant magnetic stirring for 15 min. As a final step, the product was collected by centrifugation, washed twice with water and once with ethanol, and then kept inside the oven for drying at 60 °C. NiSe was synthesized using different ligands such as oxalic acid, succinic acid, citric acid, malic acid, propionic acid, ethylene diamine, and ethylene glycol (Fig. 1a). The structures of the ligands are shown in Fig. 2a.

2.2 Synthesis of NiCoSe

Briefly, 0.5 mmol $NiCl_2$, 0.5 mmol $CoCl_2$, and 1 mmol tartaric acid were dissolved in 20 mL of deionized water. A clear solu-

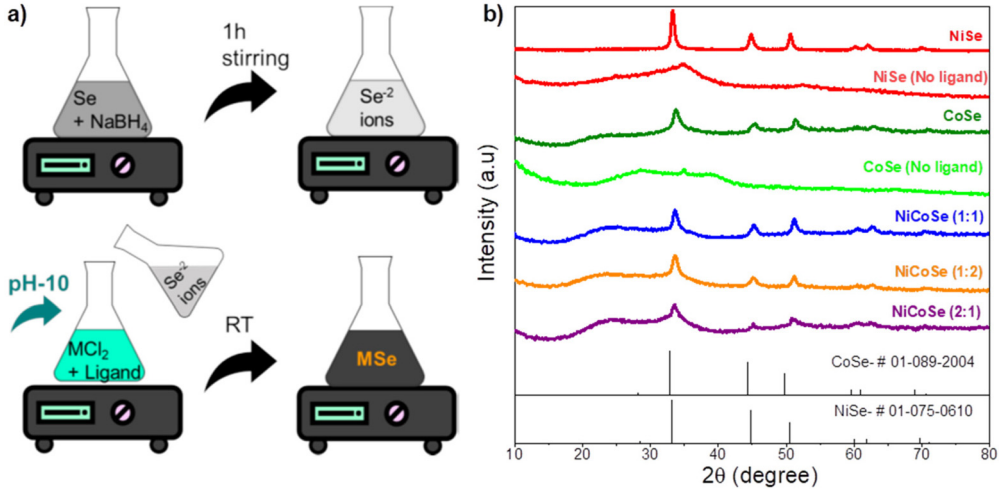

Fig. 1 (a) Synthesis scheme of MSe (M = Ni, Co) synthesized with ligands. (b) PXRD patterns of NiCoSe synthesized with different Ni : Co ratios.

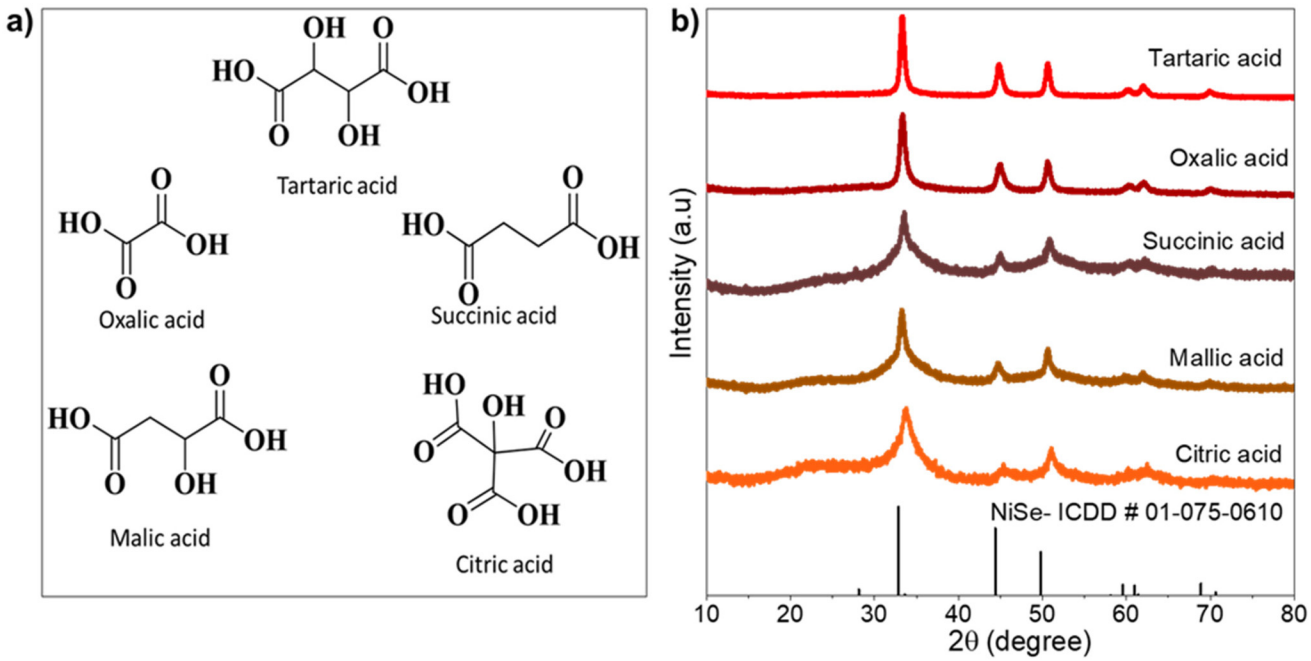

Fig. 2 (a) Structures of the ligands used. (b) PXRD patterns of the synthesized materials with different carboxylic acid-containing ligands confirmed the formation of the crystalline NiSe phase.

tion of 2 mmol Se and 2 mmol $NaBH_4$ was prepared by stirring for 45 min under mild heating conditions. Thereafter, the as-prepared metal solution and Se solution were added under constant magnetic stirring for 15 min to get a black precipitate. Finally, the product was collected by centrifugation, washed twice with water and once with ethanol, and then kept inside the oven for drying at 60 °C. NiCoSe with 1 : 2 and 2 : 1 Ni : Co precursor ratios was also synthesized using a similar protocol. For ease of understanding, NiCoSe with Ni : Co = 1 : 1, 1 : 2, and 2 : 1 is represented as NiCoSe (1 : 1), NiCoSe (1 : 2), and NiCoSe (2 : 1), respectively.

3. Results and discussion

3.1. Phase analysis

To determine the phase of the as-synthesized materials, powder X-ray diffraction (PXRD) analysis was performed (Fig. 1b). The PXRD results confirm that the material synthesized in the presence of tartaric acid as a ligand resulted in the formation of pure phases of NiSe and CoSe. In contrast, the PXRD pattern of the material synthesized in the absence of any ligand under similar reaction conditions shows an amorphous nature. This suggests that the ligand tartaric acid plays

a role in tuning the phase of the as-synthesized materials. The PXRD patterns of the materials synthesized with different Ni : Co ratios, such as NiCoSe (1 : 1), NiCoSe (1 : 2), and NiCoSe (2 : 1), are found to match well with the standard patterns of CoSe and NiSe phases. However, there is no evidence of peak splitting or additional reflections that would suggest the coexistence of distinct NiSe and CoSe phases. Instead, the diffraction pattern displays consistently shifted peak positions relative to the parent phases, indicating the formation of a homogeneous solid solution. This shift is attributed to the substitution of Co^{2+} ions into the NiSe lattice, which introduces lattice strain and alters the unit cell parameters. Such behavior is consistent with previous reports, including the study by Jiang *et al.*,[39] where the incorporation of Ni into Co-based selenides resulted in noticeable peak shifts, confirming solid solution formation rather than phase separation.

3.2. Growth mechanism

To understand the role of functional groups in the ligand, nickel selenide was synthesized using different dicarboxylic acid-containing ligands such as oxalic acid, succinic acid, citric acid, and malic acid. Interestingly, the PXRD patterns shown in Fig. 2b of the as-synthesized materials indicate that the materials synthesized with carboxylic acid-containing ligands possess the crystalline NiSe phase. To further confirm the role of dicarboxylic acid-containing ligands, we synthesized the materials with ligands containing monocarboxylic acid (propionic) and other bidentate (ethylene diamine and ethylene glycol) functional groups. The resulting PXRD patterns shown in Fig. S1 depict that the as-synthesized material did not show NiSe phase formation; instead, peaks corresponding to the selenium impurity are observed. These results confirm that ligands possessing dicarboxylic groups play an important role in the formation of the crystalline NiSe phase. It is likely that the utilization of carboxylic ligands influences the nucleation and growth of crystals *via* steric hindrance or electrostatic interactions. Ligands with specific chemical functionalities, such as chelating groups or coordination sites, can act as catalysts, lowering the energy barrier for crystallization and facilitating the transformation process. Moreover, these ligands play a pivotal role in impeding the reamorphization of materials by stabilizing the crystalline phase. Generally, higher temperatures can help overcome the energy barrier for crystallization by providing the necessary energy to break existing bonds and allow the formation of new, more ordered bonds associated with a crystalline structure. To validate this phenomenon, the precursor was subjected to heating at 70 °C without a ligand and with ethylene diamine. The PXRD pattern shows that the material without a ligand and with ethylene diamine synthesized at 70 °C has a crystalline NiSe phase (Fig. S2). Heating generally increases the mobility of molecules and promotes crystallization by providing the necessary energy to overcome kinetic barriers. Similarly, the ligands act as catalysts in these reactions, effectively lowering the energy barrier for crystallization and aiding in the transformation process. These results contribute to the understanding of the factors influencing crystallization processes and provide valuable insights for the rational design and synthesis of functional materials with tailored properties.

3.3. Computational studies for growth mechanism

Computations were carried out to shed light on these experimental results. Experiments show that the nickel selenide crystal structure emerges only from certain Ni(II) complexes and not others. In particular, the oxalate and tartrate complexes of nickel provide conducive pathways toward the formation of nickel selenide crystals. By contrast, the ethylene diamine complex of Ni(II) yields an amorphous product when reacted with the selenide precursor. The computations aimed to explain why certain complexes of Ni(II) followed a desired pathway to form nickel selenide crystals while other complexes did not. As a case study, three complexes of Ni(II) were chosen for computational investigations, namely, nickel-tartrate $[Ni(TAR)(H_2O)_4]$, nickel-oxalate $[Ni(OXAL)(H_2O)_4]$ and nickel-ethylene diamine $[Ni(EN)_3]^{2+}$. The complexes' geometries were optimized, and the optimized structures of the three complexes were obtained and are shown in Fig. S3 for $[Ni(EN)_3]^{2+}$, Fig. S4 for $[Ni(TAR)(H_2O)_4]$ and Fig. S5 for $[Ni(OXAL)(H_2O)_4]$. Owing to the negative charge on each carboxylate group, the two carboxylate complexes are charge-neutral. The nickel-ethylene diamine complex is cationic, carrying a 2+ charge because EN is a neutral ligand. Further, it can be observed that in the $[Ni(TAR)(H_2O)_4]$ and $[Ni(OXAL)(H_2O)_4]$ complexes, there exist hydrogen bonding interactions between the oxygen atoms of the carboxylate ligands and the hydrogen atoms of the water molecules in the complex. There are two such interactions in the $[Ni(TAR)(H_2O)_4]$ complex (Fig. S4) and three hydrogen bonding interactions in the $[Ni(OXAL)(H_2O)_4]$ complex (Fig. S5). The interaction distances are indicated in the insets of the respective figures. These hydrogen bonding interactions serve to stabilise the nickel carboxylate complexes in the optimized configuration.

Table S1 shows the binding free energy of formation for the $[Ni(TAR)(H_2O)_4]$, $[Ni(OXAL)(H_2O)_4]$, and $[Ni(EN)_3]^{2+}$ complexes from their aqueous complexes in the solution. The experimental conditions were considered, and an aqueous medium was simulated in the initial nickel species and in the medium of the reaction. The equations employed for the calculation of the binding free energy for the three complexes are as follows:

$$\Delta E_f[Ni(TAR)(H_2O)_4] = E[Ni(TAR)(H_2O)_4] + 2E[H_2O] - E[Ni(H_2O)_6]^{2+} - E[TAR]^{2-} \quad (1)$$

$$\Delta E_f[Ni(OXAL)(H_2O)_4] = E[Ni(OXAL)(H_2O)_4] + 2E[H_2O] - E[Ni(H_2O)_6]^{2+} - E[OXAL]^{2-} \quad (2)$$

$$\Delta E_f[Ni(EN)_3]^{2+} = E[Ni(EN)_3]^{2+} + 6E[H_2O] - E[Ni(H_2O)_6]^{2+} - 3E[EN] \quad (3)$$

A negative value of the calculated binding energy indicates that the formation of the complex is favorable, and a positive value indicates the opposite. As shown in Table S1, all three complexes have a favorable energy of formation from the aqueous

medium. The $[Ni(EN)_3]^{2+}$ complex has the most negative binding energy of approximately −100 kcal mol^{-1}, whereas the carboxylate complexes have about a fourth of that energy. This means that the $[Ni(EN)_3]^{2+}$ complex is highly stable. The reason for this may be that the entropy change associated with the formation (eqn (3)) is significantly different. Six water molecules are released in the formation of the $[Ni(EN)_3]^{2+}$ complex as compared to the two water molecules released in the case of the carboxylate complexes. The positive change in entropy associated with the formation of the former renders it more stable.

During experiments, it was observed that the $[Ni(EN)_3]^{2+}$ complex is not a good precursor for the formation of the nickel selenide crystal structure at room temperature. On the contrary, the two carboxylate complexes are suitable precursors, enabling the formation of nickel selenide crystals at room temperature. The reason for this is likely to be that the high stability of the $[Ni(EN)_3]^{2+}$ complex, compared with the carboxylate complexes, makes it less favorable to break and allows selenium to approach the nickel center. Interestingly, at elevated temperatures, the $[Ni(EN)_3]^{2+}$ complex has been observed to facilitate nickel selenide crystal formation. If the reaction switches to spontaneous at higher temperatures, this indicates that the reaction relies significantly on entropic factors. In the expression for free energy ($\Delta G = \Delta H - T\Delta S$), the free energy ΔG becomes more negative at higher temperatures when the change in entropy ΔS is positive. The change in entropy is greater when the carboxylate complexes are turned into nickel selenide crystals. Four water molecules and one tartrate/oxalate ligand are displaced in these cases. By contrast, if the $[Ni(EN)_3]^{2+}$ complex breaks, three EN ligands are freed from the complex. Hence, the change in entropy is less in the case of the $[Ni(EN)_3]^{2+}$ complex than in the cases of the two carboxylate complexes. Consequently, only when the temperature is increased, the breaking of the $[Ni(EN)_3]^{2+}$ complex tips the free energy balance from positive to negative, thus rendering this reaction spontaneous at higher temperatures.

Computational studies reveal that the $[Ni(EN)_3]^{2+}$ complex exhibits significantly higher stability than the carboxylate-based complexes. This enhanced thermodynamic stability reduces the likelihood of ligand dissociation, thereby limiting the accessibility of the nickel center to incoming selenium species. As a result, the formation of nickel selenide crystals from this complex is unfavorable under ambient conditions. In contrast, the nickel-tartrate and nickel-oxalate complexes possess moderate binding energies and are further stabilized by hydrogen bonding interactions between coordinated water molecules and carboxylate oxygen atoms. These interactions promote a more flexible coordination environment, facilitating the approach and incorporation of selenium into the nickel coordination sphere. Consequently, these carboxylate complexes act as effective precursors for nickel selenide crystal formation at room temperature. In the absence of dicarboxylic acid ligands, the lack of such stabilizing interactions and poor precursor integrity often result in incomplete reaction pathways, leading to the presence of unreacted elemental selenium in the final product, as confirmed by XRD analysis.

3.4. Thermogravimetric analysis

To support our theoretical hypothesis, we synthesised the reaction intermediate complexes nickel-tartrate $[Ni(TAR)(H_2O)_4]$, nickel-oxalate $[Ni(OXAL)(H_2O)_4]$, and nickel-ethylene diamine $[Ni(EN)_3]^{2+}$ and performed thermogravimetric analysis (TGA) (synthesis details are available in the SI). As shown in Fig. S6a and b, the TGA curves of the Ni–OXAL and Ni–TAR complexes display a clear weight loss between 120 °C and 300 °C, which corresponds to the release of coordinated water molecules. Interestingly, the Ni–EN complex does not show any noticeable change in this range, indicating the absence of such water loss. This implies that the Ni–EN complex is inherently more stable, and because of this stability, its ligands are less likely to detach. As a result, the nickel center is less accessible to incoming selenium species, making the formation of nickel selenide crystals from this complex unlikely under normal conditions. These findings are in strong agreement with the predictions of our theoretical calculations.

3.5. FTIR analysis

To understand the nature of the interaction between ligand molecules and the as-synthesized nickel selenides, we compared the FT-IR spectra of nickel selenides with the corresponding spectra of pure oxalic acid and tartaric acid. The FTIR spectrum of oxalic and tartaric acid-capped NiSe shows the characteristic peaks of the functional groups of the ligands. This confirms the attachment of ligands, possibly at the surface of nickel selenide. For oxalic acid-capped NiSe, the peak corresponding to the –C═O stretching frequency of the carboxylic group is observed at 1637 cm^{-1}, whereas for the pure ligand, the corresponding peak is observed at 1679 cm^{-1} (shown in Fig. S7a).[33,40] For tartaric acid-capped NiSe, the peak belonging to the –C═O stretching frequency is observed at 1724 cm^{-1} and that of the ligand is observed at 1740 cm^{-1} (shown in Fig. S7b).[41,42] In oxalic and tartaric acid-capped NiSe, the –C═O peak of the carboxylic acid shifts to relatively lower wavelengths. These spectroscopic changes suggest that oxalic and tartaric acids are attached to the nickel selenide surface through the carboxyl functional moiety.

3.6. Morphological analysis

The morphology of the as-prepared samples was analyzed by scanning electron microscopy (SEM) and transmission electron microscopy (TEM). The SEM images show that NiSe and CoSe particles have an irregular sphere-like morphology (shown in Fig. S8a–d). For both NiSe and CoSe, smaller particles with a size of ∼40 nm are aggregated to form the spherical particles. Similar observations are found from the corresponding TEM images (shown in Fig. S8e and f). The calculated d spacing value measured from the HRTEM image of nickel selenide is 0.27 nm, corresponding to the (101) plane of NiSe. Similarly, for CoSe particles, the d spacing value is estimated to be 0.26 nm, which corresponds to the (101) plane of CoSe (shown in Fig. S8g and h). The SEM and TEM images shown in Fig. S9a, b and d–f depict that the as-synthesized NiCoSe

materials have a similar spherical morphology to CoSe and NiSe particles. NiCoSe materials are composed of spherical particles with a size of 45 nm. Hardly any change in the morphology is noted for NiCoSe prepared with different Ni-to-Co ratios. The calculated d spacing value measured from the HRTEM image of NiCoSe (1 : 1) (Fig. S9c) is 0.27 nm, corresponding to the (101) plane. To understand the spatial distribution of elements, the elemental mapping (shown in Fig. S9g–j) of the as-synthesized materials was performed. Elemental mapping images show the uniform distribution of elements (Ni, Co, and Se) in nickel cobalt selenide. To determine the elemental compositions, the EDAX analysis of the as-synthesized materials was carried out. The observed experimental ratios obtained from the atomic ratios of cobalt, nickel, and selenium for different samples are similar to the theoretical ratios (Table S2).

3.7. XPS analysis

The chemical states of different elements in the materials were further investigated by XPS analysis. The survey spectrum depicted in Fig. S10a confirms the existence of Co, Ni, Se, and O in the NiCoSe (1 : 1) material. As shown in Fig. S10b, the peaks observed at 855.6 eV (Ni $2p_{3/2}$) and 873.1 eV (Ni $2p_{1/2}$) can be attributed to Ni^{2+}, while the peaks present at 858.4 eV (Ni $2p_{3/2}$) and 876 eV (Ni $2p_{1/2}$) are attributed to Ni^{3+}.[43,44] The peaks at 778 eV (Co $2p_{3/2}$) and 793.6 eV (Co $2p_{1/2}$) in the Co 2p spectrum (shown in Fig. S10c) are attributed to Co^{3+}. The peaks at 781 eV (Co $2p_{3/2}$) and 803 eV (Co $2p_{1/2}$) are characteristics of the Co^{2+} species.[23,45] The broad peak at 59 eV in the Se 3d spectrum (shown in Fig. S10d) is associated with the oxidized selenium species (SeO_x) as a result of surface oxidation. The two peaks at 54.3 eV and 55.3 eV belong to Se $3d_{5/2}$ and Se $3d_{3/2}$, respectively.[46,47] All these results confirm the coexistence of Ni and Co in the as-synthesized NiCoSe (1 : 1) material.

4. Electrochemical activity evaluation

4.1. Hydrazine oxidation reaction

The electrocatalytic HzOR activity of the as-synthesized materials was evaluated in 1 M KOH. Fig. 3 shows the LSV curves of NiSe in a hydrazine-free electrolyte with different concentrations of hydrazine (0.1, 0.2, 0.3, 0.4, and 0.5 M). In the electrolyte without hydrazine (0 mM), the LSV curve in the potential range of interest (0.1 to 1 V *vs.* RHE) does not show any observable redox current. However, in a 0.1 M hydrazine solution, the anodic current increases to ~0.15 V *versus* RHE (shown in Fig. 3a) and continues to increase with increasing concentrations of hydrazine. This confirms hydrazine as the substrate in the observed results. Further, the electrochemical performance of NiSe, CoSe, and NiCoSe catalysts was investigated. The LSV curve shown in Fig. 3b indicates that NiCoSe (1 : 1) requires a potential of 0.20 V *vs.* RHE to reach a 10 mA cm^{-2} current density. The corresponding potential values for CoSe and NiSe are 0.30 and 0.40 V *vs.* RHE, respectively. These results show that the bimetallic NiCoSe phase shows superior activity to individual NiSe and CoSe phases. Among the as-synthesized NiCoSe materials, NiCoSe (1 : 1) requires the lowest potential to attain 10 mA cm^{-2} compared to NiCoSe (1 : 2) (0.30 V *vs.* RHE) and NiCoSe (2 : 1) (0.38 V *vs.* RHE). Furthermore, a high current density of 300 mA cm^{-2} is attained at a potential of 700 mV without the use of any electrochemically active substrate, like Ni foam. Further electrochemical measurements were carried out using the NiCoSe (1 : 1) catalyst because it shows the best activity. The higher activity of NiCoSe is supported by a low Tafel slope of 65 mV dec^{-1} compared to CoSe (113 mV dec^{-1}) and NiSe (184 mV dec^{-1}) (shown in Fig. 3c). The observed lower Tafel slope for NiCoSe (1 : 1) suggests the faster kinetics of the electrochemical reactions on the NiCoSe catalyst.

Electrochemical impedance spectroscopic (EIS) analysis was performed at 0.3 V *vs.* RHE in 0.5 M hydrazine to understand the possible origin of the higher activity of the NiCoSe electrocatalyst. The observed charge transfer resistance (R_{CT}) of NiCoSe (~11.5 Ω) is lower than that of CoSe (~50.5 Ω) and NiSe (~71.5 Ω) (Fig. 3d). The ECSA measurement was performed to get a better insight into the developed catalyst.[48,49] It is generally believed that the electrocatalytic activity of materials increases with an increase in their ECSA. However, due to the limitations of all the existing methods, the accurate determination of the ECSA is extremely challenging. Therefore, a qualitative comparison of the ECSA of the as-synthesized materials was obtained from the double-layer capacitance (C_{dl}) of materials measured in the non-faradaic region. The calculated C_{dl} value of NiSe (11.8 mF cm^{-2}) is higher than those of CoSe (6.8 mF cm^{-2}) and NiCoSe (2.0 mF cm^{-2}) (shown in Fig. S11a–d). To find the intrinsic activity, the LSV curves were normalized by the ECSA (shown in Fig. S11e). Despite having the lowest ECSA, NiCoSe exhibits the highest current density when normalized by the ECSA, indicating superior intrinsic catalytic activity towards hydrazine oxidation compared to both NiSe and CoSe. This enhanced performance is attributed to the synergistic effect between Ni and Co in the bimetallic structure, which improves the electronic environment and reaction kinetics.[50] Thus, we believe that the enhanced activity of NiCoSe is very likely due to the presence of more potent catalytic centers that can catalyze reactions with higher efficiency. Further, the durability of NiCoSe for the HzOR was analyzed using chronopotentiometry measurements. As shown in Fig. S12a, NiCoSe shows excellent stability of 32 h at a current density of 10 mA cm^{-2}. The HzOR performance shows a significant rise in the potential requirement in 16 h. As previously noted in the literature, the rise in potential requirements may result from either the electrocatalyst deterioration or the consumption of hydrazine during the HzOR.[12,51] After 16 hours, the electrolytic solution was swapped for a fresh one to confirm the reason for the increment in the potential requirement. The electrochemical performance of NiCoSe for the HzOR is restored and displays a similar trend for another 16 hours. To further validate the stability of the hydrazine oxidation reaction (HzOR), the linear sweep voltammetry (LSV) curves were recorded before and after the chronopotentiometry

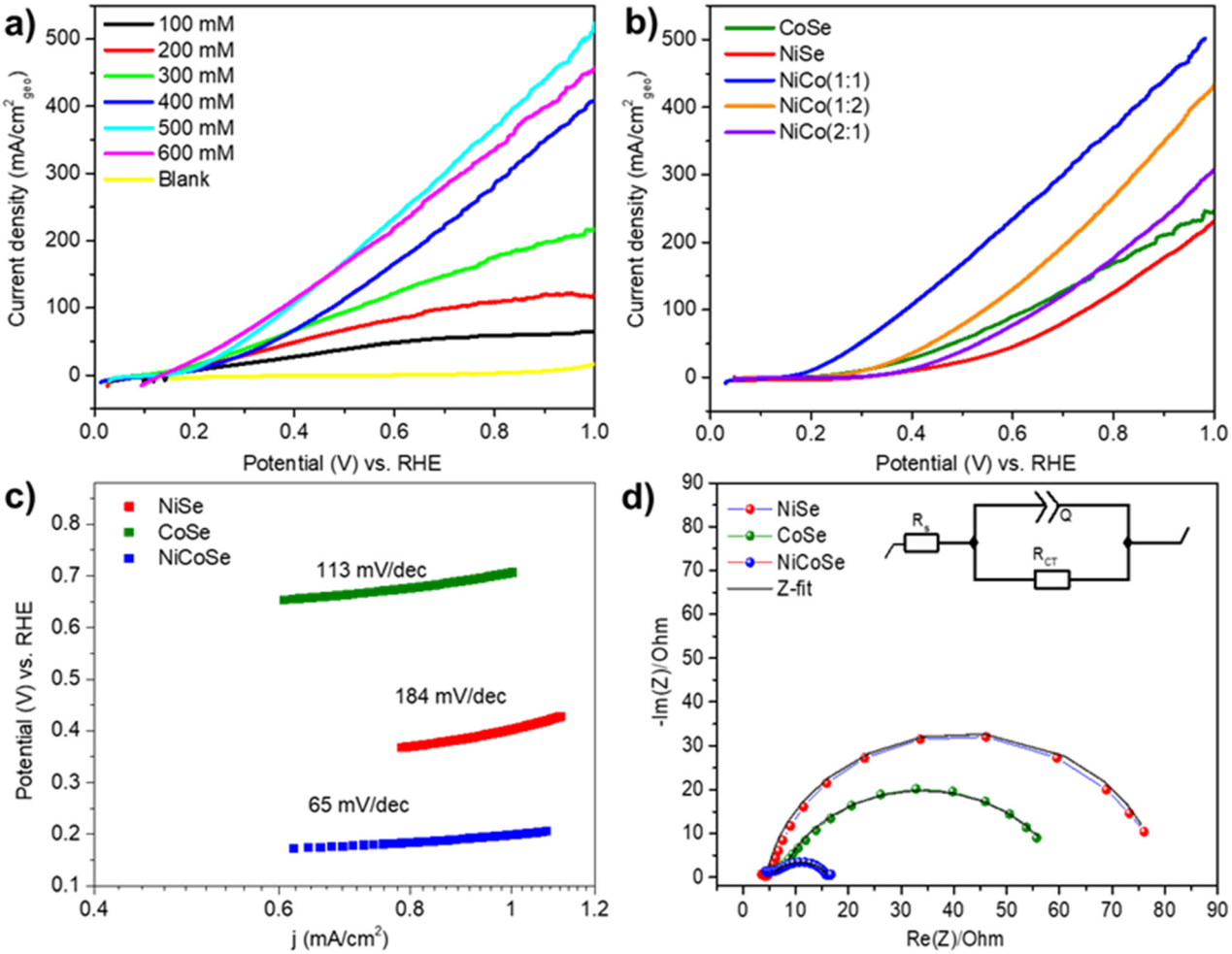

Fig. 3 Electrochemical performance towards the HzOR. (a) LSV curves of NiCoSe (1 : 1) without Hz and with different hydrazine concentrations. (b) LSV curves of the as-synthesized materials towards hydrazine oxidation at a scan rate of 5 mV s^{-1} in a 0.5 M Hz + 1 M KOH electrolyte. (c) Tafel plots estimated for the as-synthesized metal selenides. (d) The EIS curves measured at 0.30 V *vs.* RHE.

test in a fresh electrolyte containing 0.5 M Hz + 1 M KOH. The negligible change in the LSV profile confirms the excellent electrochemical stability of the NiCoSe catalyst during prolonged HzOR operation (shown in Fig. S12b). It confirms that the consumption of hydrazine leads to a decrease in activity; however, the electrocatalyst is stable

4.2 Hydrogen evolution reaction

The HER performance of the as-synthesized metal selenides was measured in a three-electrode cell configuration using 1 M KOH as the electrolyte. We used the backward polarization curves to evaluate the electrocatalytic performance, as they are devoid of any contribution from the capacitance and metal redox processes in the potential range of interest (Fig. 4a). The geometric catalytic HER activity of NiCoSe is found to be higher than that of CoSe and NiSe in 1 M KOH. To attain a current density of 10 mA cm^{-2}, an overpotential of 200 mV is required for NiCoSe, while CoSe and NiSe require 230 mV and 260 mV, respectively. The Tafel slope was estimated to get an insight into the kinetics of HER activity (Fig. 4b). The NiCoSe catalyst is found to have a lower Tafel slope value of 112 mV dec^{-1} than CoSe (147 mV dec^{-1}) and NiSe (140 mV dec^{-1}). These Tafel slope values are significantly different from the widely noted values (derived from the Butler–Volmer equation at $\theta = 0$). This is possible only if the Heyrovsky step is the rate-determining step in the HER.[52]

To further support the higher activity of NiCoSe compared with that of NiSe and CoSe, electrochemical impedance spectroscopy was performed at −0.20 V *vs.* RHE. The observed charge transfer resistance (R_{CT}) value is lower for NiCoSe (~9.1 Ω) than for NiSe (~11 Ω) and CoSe (~16.5 Ω) catalysts (see Fig. 4c). These results show that the superior activity of NiCoSe is due to faster kinetics, as reflected by the low R_{CT} and Tafel slope. Additionally, the intrinsic activity of the synthesized catalyst toward the HER was calculated by ECSA-normalized LSV. Fig. S11f shows the electrochemically active surface area (ECSA)-normalized polarization curves for the hydrogen evolution reaction. NiCoSe exhibits the highest

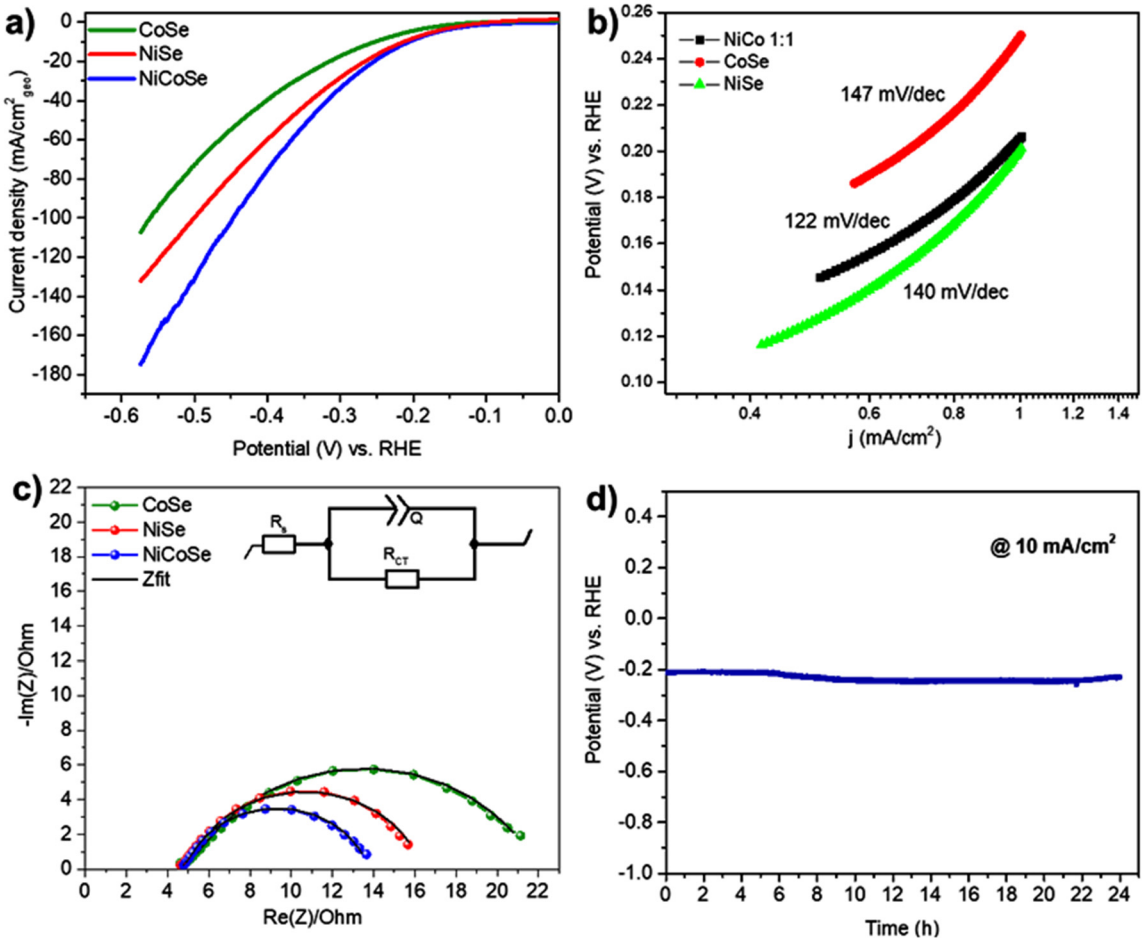

Fig. 4 Electrocatalytic performance for the HER in 1 M KOH: (a) linear sweep voltammetry (LSV) curves of NiSe, CoSe, and NiCoSe (1 : 1, 1 : 2, and 2 : 1), representing the geometric activity. (b) The corresponding Tafel plots. (c) EIS curves measured at −0.2 V *vs.* RHE. (d) Chronopotentiometric curve of NiCoSe (1 : 1) for the HER.

current density when normalized by the ECSA, indicating superior intrinsic catalytic activity compared to both NiSe and CoSe. Further, the durability of the best-performing HER electrocatalyst (NiCoSe) was evaluated by performing a 24 h chronopotentiometric analysis at 10 mA cm^{-2}_{geo} in 1 M KOH (Fig. 4d). The HER performance of NiCoSe (1 : 1) under continuous usage displays a negligible decrease even after 24 h, demonstrating the prominent durability.

Further, we have compared the catalytic performance of the NiCoSe catalyst with commercial Pt/C for the HzOR and HER. The polarization curves of commercial Pt/C in both the hydrazine oxidation reaction (HzOR) and hydrogen evolution reaction (HER) are shown in Fig. S13a and c. The NiCoSe catalyst exhibits a higher overpotential than Pt/C. Also, Pt/C exhibits a lower Tafel slope of 43 mV dec^{-1} in the HER compared to the 122 mV dec^{-1} measured for NiCoSe, suggesting faster HER kinetics in the case of Pt/C (shown in Fig. S13b). However, in the case of the HzOR, NiCoSe demonstrates a Tafel slope of 65 mV dec^{-1}, which is reasonably close to the 48 mV dec^{-1} observed for Pt/C (shown in Fig. S13d). This suggests that NiCoSe possesses competitive intrinsic activity for the HzOR. Also, NiCoSe is composed of earth-abundant and low-cost materials, offering a more economically viable alternative for scalable applications. NiCoSe can be a promising alternative for scalable energy systems due to its high durability and affordability.

Furthermore, we have checked the OER performance of the NiCoSe catalyst. The LSV curve shows that the anodic potential for water oxidation is 1.62 V *vs.* RHE at 10 mA cm^{-2}. An excess potential of 1.42 V is required for water oxidation in the conventional water electrolysis system (Fig. 5a). However, the HzOR can deliver a much higher current density than the OER at a low work potential, which depicts the significantly enhanced energy efficiency by replacing the OER with the HzOR. The above results depict that the NiCoSe catalyst is an efficient catalyst for the HzOR and HER. Thus, we checked the bifunctional activity of NiCoSe toward hydrazine-assisted water splitting (OHzWS) and compared its activity with the traditional overall water splitting system (OWS). For the electrochemical measurements, we used a NiCoSe electrode as the cathode and anode in a two-electrode setup for the overall water splitting. To attain a current density of 10 mA cm^{-2}_{geo}, the NiCoSe||NiCoSe couple requires a cell potential of 0.45 V

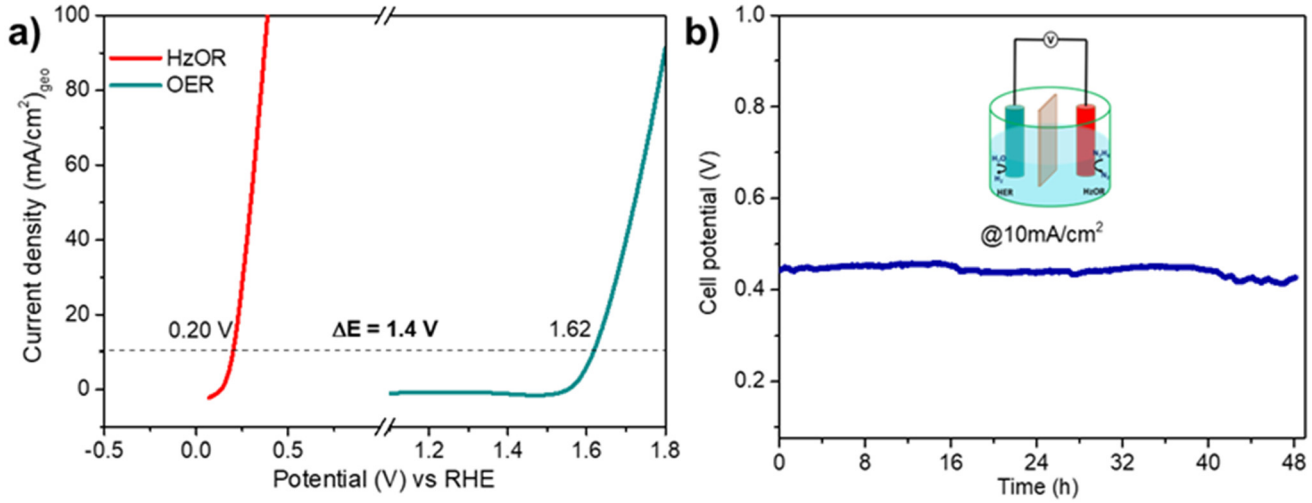

Fig. 5 Electrocatalytic performance of the bifunctional catalyst: (a) LSV curves of the hydrazine electrolysis (HzOR) (1.0 M KOH with 0.5 M hydrazine) and OER (1.0 M KOH). (b) Chronopotentiometric curve to get a current density of 10 mA cm^{-2}_{geo} in 1.0 M KOH with 0.5 M hydrazine (blue line). The inset shows the schematic setup of the two-electrode system.

in an electrolyte containing 0.5 M hydrazine and 1 M KOH and outperforms OWS (an electrolyte containing 1 M KOH), which requires 1.81 V (shown in Fig. S14). To understand the durability of the NiCoSe catalyst, a chronopotentiometry test was employed for 48 h at 10 mA cm^{-2}. The bifunctional activity of NiCoSe under continuous usage shows a negligible decrease even after 48 h, demonstrating good durability in the two-electrode system (shown in Fig. 5b). To determine the rate of hydrogen production, the chronoamperometry (CA) measurement was performed at 0.85 V using the NiCoSe||NiCoSe couple, and hydrogen was detected at different reaction times with the help of an online gas chromatography setup. The hydrogen production rate is initially measured as 27 mL h^{-1} (2 min), which decreases to 22.1 mL h^{-1} (32 min) and 18.6 mL h^{-1} (56 min) with an increase in the reaction time, which is due to the consumption of hydrazine during the reaction, a common phenomenon observed in the case of hydrazine oxidation-assisted hydrogen production (Table S4 and Fig. S15). The above results show that the NiCoSe system, under alkaline conditions, is a promising electrocatalyst to promote hydrazine-assisted hydrogen production. Additionally, NiCoSe shows better electrochemical performance and stability than most of the reported chalcogenide-based bifunctional catalysts for OHzWS (Table S5).

5. Computational findings on the HzOR mechanism

The hydrazine oxidation reaction (HzOR) experimentally carried out on NiSe and NiCoSe (1 : 1) has been simulated using density functional theory calculations. In NiCoSe (1 : 1), half the Ni atoms are replaced by Co in the lattice. The simulations elaborate on the experimental findings pertaining to the electrochemical properties of the material surfaces. Based on the XRD results, the [1 0 1] planes of NiSe and NiCoSe (1 : 1) have been considered as the catalytic plane.

The experiments have demonstrated the feasibility of the HzOR on the NiSe and NiCoSe (1 : 1) surfaces. Calculations were performed to investigate the free energy associated with the stepwise mechanism of the HzOR on both surfaces. The two energy profiles are overlaid in Fig. 6 for effective comparison. The [1 0 1] planes of NiSe (blue) and NiCoSe (1 : 1) (pink) have been considered for the binding of hydrazine and its oxidized successors. Fig. 6 shows the reaction pathways and corresponding energy changes for the HzOR on the two surfaces. The free energy profiles of the HzOR on the NiSe (blue) and NiCoSe (1 : 1) (pink) surfaces as a function of the reaction coordinate are shown. The profile labels are shown in the inset. Optimized geometries focused on the active site of binding are provided along the reaction pathway for both surfaces. The experiments have been performed under high-pH conditions. The following equations have been employed for the free energy calculations in alkaline media:

$$N_2H_4 + * \rightarrow *N_2H_4 \quad (1)$$

$$*N_2H_4 + OH^- \rightarrow *N_2H_3 + H_2O + e^- \quad (2)$$

$$*N_2H_3 + OH^- \rightarrow *N_2H_2 + H_2O + e^- \quad (3)$$

$$*N_2H_2 + OH^- \rightarrow *N_2H_1 + H_2O + e^- \quad (4)$$

$$*N_2H_1 + OH^- \rightarrow *N_2 + H_2O + e^- \quad (5)$$

$$*N_2 \rightarrow N_2{}^+* \quad (6)$$

where * represents an adsorbed species.

The materials are similar to each other in terms of their structures and unit cell geometries. The differences between the two are that in NiCoSe (1 : 1) (pink), half of the Ni atoms

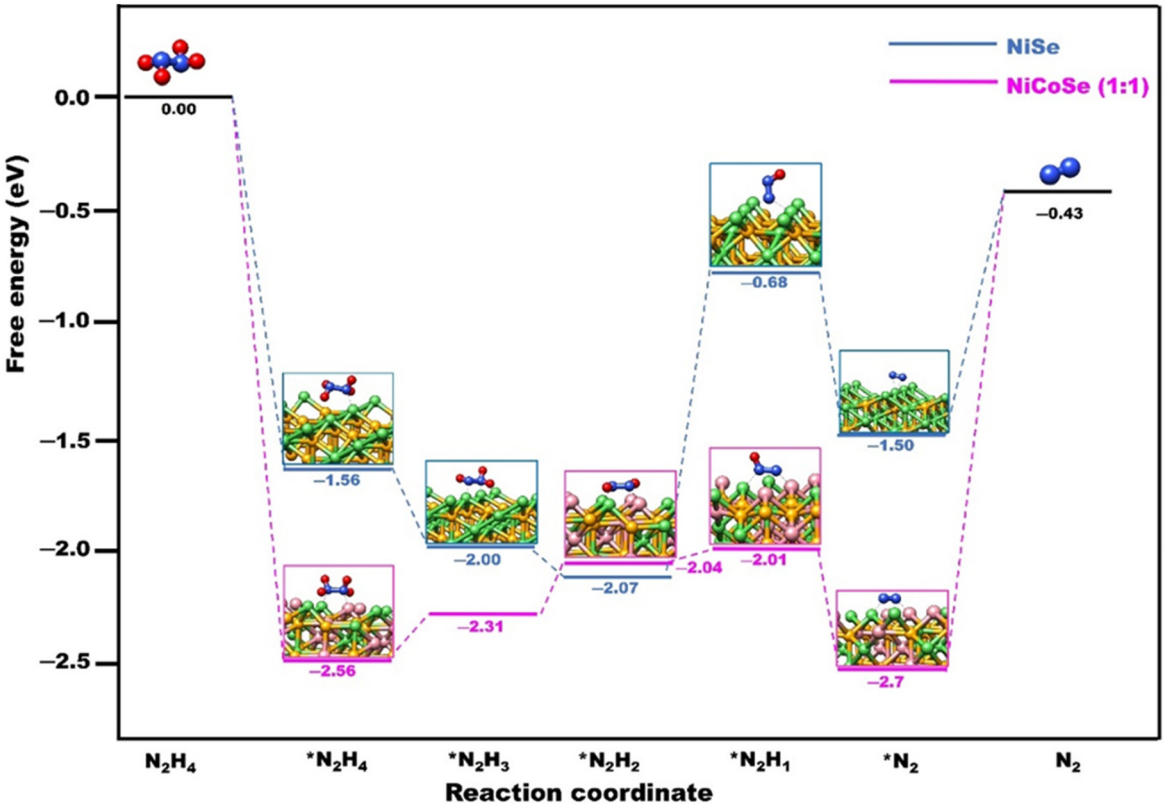

Fig. 6 Reaction pathways and corresponding energy changes for the HzOR. The free energy profiles of the HzOR on the NiSe (blue) and NiCoSe (1 : 1) (pink) surfaces as a function of the reaction coordinate. The profile labels are shown in the inset. Optimized geometries focused on the active site of binding are provided along the reaction pathway for both surfaces.

are replaced by Co. It is evident from Fig. 6 that a step with a rise in free energy is a rise for both, and a step with a drop is so for both. As observed in the experiments, both are viable and good materials for the HzOR. This matches the result obtained in the calculations, showing a net negative free energy change for both materials. In nearly all the steps of the mechanism, the potential for NiCoSe (1 : 1) is lower than that for NiSe. Additionally, the adsorption of N_2H_4 onto the catalytic surface is more favorable in the case of NiCoSe (1 : 1). In turn, the desorption of N_2 in the last step requires more energy in the case of NiCoSe (1 : 1). These are reflected in the changes in the free energy between the adsorbed and desorbed species in both cases. The step of $*N_2H_2$ becoming $*N_2H_1$ is of particular interest. At this transition, in the case of NiSe, the rise in the energy is high, whereas for NiCoSe (1 : 1), the ΔG difference is lower. These three factors combined render the overall HzOR mechanism to be more favorable on the NiCoSe (1 : 1) surface as compared to the NiSe surface. These results corroborate the experimental findings.

6. Post-catalysis studies

It is known that an electrocatalyst may undergo structural changes after being subjected to long electrocatalytic cycles. To understand the occurrence of any such transformation during electrocatalysis, the NiCoSe (1 : 1) electrodes were subjected to post-catalytic analyses after 10 h of chronopotentiometry. The post-catalytic PXRD pattern of NiCoSe (1 : 1) illustrated in Fig. S16a confirms the retention of the phase after the durability test. The XPS spectra of the Ni 2p, Co 2p, and Se 3d regions of NiCoSe (1 : 1) do not show any shift in the binding energy compared to the pre-catalytic sample (Fig. S16b–d). All these results confirm that NiCoSe is a robust and efficient catalyst for hydrazine oxidation.

7. Conclusions

In conclusion, a facile one-step ligand-assisted room-temperature route was developed to synthesize pure-phase NiSe, CoSe, and NiCoSe materials. This was achieved by reacting metal salts with elemental Se in the presence of dicarboxylic acid molecules like tartaric acid. The role of functional groups in ligands was probed, and it was found that carboxylic acid groups played a key role in the synthesis of nickel and cobalt selenides. The computations optimized the stable geometries and geometric parameters of the nickel complexes with tartaric, oxalate, and ethylene diamine ligands. Binding energy calculations under experimental conditions revealed the higher

likelihood of the carboxylate complexes forming crystalline NiSe compared to the $[Ni(EN)_3]^{2+}$ complex at room temperature. The importance of entropic effects was discussed, and the formation of NiSe from the $[Ni(EN)_3]^{2+}$ complex was predicted at high temperatures. This prediction was validated by experimental findings. Among the synthesized metal selenides, bimetallic NiCoSe exhibited excellent activity toward hydrazine oxidation (0.20 V *vs.* RHE). To drive a high current density of 300 mA cm^{-2}, the developed NiCoSe required a potential of 700 mV without the assistance of electrochemically active substrates such as Ni foam or Co foam. Moreover, NiCoSe showed excellent bifunctional activity, and it required a very low cell voltage of 0.45 V to attain a current density of 10 mA cm^{-2}. The computational results revealed a similar profile for both materials and the enhanced feasibility of the HzOR on the NiCoSe (1 : 1) compared to NiSe. The thermodynamic advantages lie in the stronger adsorption of species on the NiCoSe (1 : 1) surface, the lowered energy for each step, and the less drastic energy changes between one step and the next in the case of NiCoSe (1 : 1).

Author contributions

A. E. Praveen, V. Mishra, and V. Mahalingam have conceptualized the study. A. E. Praveen and V. Mishra performed the experiments and conducted critical analysis of the experimental data. A. E. Praveen has written the original draft with the help of V. Mishra and V. Mahalingam. A. Chandrasekar planned and performed the computational studies. V. Mahalingam supervised the overall work, providing motivation and oversight throughout its execution. All authors have approved the final version of the manuscript.

Conflicts of interest

The authors have no conflicts to declare neither in the financial interests nor in the personal relationships that could have appeared to influence the work reported in this paper.

Data availability

The data that support the findings of this study are available from the corresponding author upon reasonable request.

The supplementary information file consists of instrumentation details, material details, synthesis details, electrochemical measurement details, and computational details. PXRD, SEM, TEM, HRTM, EDS, FTIR, TGA, XPS analysis for materials used for control studies, optimized geometries of nickel complexes used in computational analysis, computed binding free energy for the formation of the nickel complexes, C_{dl} and CV plot of different catalyst, table for calculated ECSA, ECSA normalized LSV for HzOR and HER, CP curve for HzOR stability, LSV after stability for HzOR, electrochemical performance of Pt/C for HzOR and HER, table for calculated H_2 production values, comparison of OHzWS and OWS for the NiCoSe || NiCoSe couple, PXRD and XPS analysis of post-catalytic samples, comparison table for NiCoSe OHzWS performance with other reported transition metal chalcogenide-based bifunctional OHzWS electrocatalysts. See DOI: https://doi.org/10.1039/d5nr02653a.

Acknowledgements

VM thanks SERB, CSIR and IISER Kolkata for providing the instrumental facilities and funding. The authors thank TEM, DST-FIST, IISER, Kolkata, for the transmission electron microscopy facility. The authors thank Prof. Sayan Bhattacharyya and A. Roy for GC measurements.

References

1 X. L. Liu, Y. C. Jiang, J. T. Huang, W. Zhong, B. He, P. J. Jin and Y. Chen, *Carbon Energy*, 2023, **5**, e367.
2 Z. X. Ge, Y. Ding, T. J. Wang, F. Shi, P. J. Jin, P. Chen, B. He, S. B. Yin and Y. Chen, *J. Energy Chem.*, 2023, **77**, 209–216.
3 Q. Qian, Y. Zhu, N. Ahmad, Y. Feng, H. Zhang, M. Cheng, H. Liu, C. Xiao, G. Zhang and Y. Xie, *Adv. Mater.*, 2024, **36**, 1–37.
4 H. Liu, Q.-L. Hong, Y.-C. Yin, F. Shi, P. Chen and Y. Chen, *Energy Mater.*, 2025, **5**, 500068.
5 L. Quan, H. Jiang, G. Mei, Y. Sun and B. You, *Chem. Rev.*, 2024, **124**, 3694–3812.
6 Y. Z. Hu, S. F. Zhang, X. Le Han and Y. Liu, *Nanoscale*, 2025, **17**, 6362–6389.
7 H. Liu, Y. Liu, M. Li, X. Liu and J. Luo, *Mater. Today Adv.*, 2020, **7**, 100083.
8 Y. Feng, S. Wang, Y. Zhu, H. Xie, Y. Zhang, M. Cheng, X. He, Y. Chen, C. Xiao, G. Zhang and Y. Xie, *Adv. Mater.*, 2025, **37**, 2506512.
9 X. Guan, Y. Sun, S. Zhao, H. Li, S. Zeng, Q. Yao, R. Li, H. Chen and K. Qu, *SusMat*, 2024, **4**, 166–177.
10 X. Liu, J. He, S. Zhao, Y. Liu, Z. Zhao, J. Luo, G. Hu, X. Sun and Y. Ding, *Nat. Commun.*, 2018, **9**, 4365.
11 Y. Tong and P. Chen, *Inorg. Chem. Front.*, 2024, 6218–6245.
12 J. Y. Zhang, H. Wang, Y. Tian, Y. Yan, Q. Xue, T. He, H. Liu, C. Wang, Y. Chen and B. Y. Xia, *Angew. Chem., Int. Ed.*, 2018, **57**, 7649–7653.
13 A. E. Praveen, V. Mishra, S. Ganguli, A. Chandrasekar and V. Mahalingam, *Inorg. Chem.*, 2023, **62**, 16149–16160.
14 Y. Chen, Z. Fan, Z. Zhang, W. Niu, C. Li, N. Yang, B. Chen and H. Zhang, *Chem. Rev.*, 2018, **118**, 6409–6455.
15 Y. Feng, X. He, M. Cheng, Y. Zhu, W. Wang, Y. Zhang, H. Zhang and G. Zhang, *Small*, 2023, **19**, 2301986.
16 Y. Xia, C. T. Campbell, B. R. Cuenya and M. Mavrikakis, *Chem. Rev.*, 2021, **121**, 563–566.
17 A. R. Fairhurst, J. Snyder, C. Wang, D. Strmcnik and V. R. Stamenkovic, *Chem. Rev.*, 2025, **125**, 1332–1419.

18 L. Li, P. Wang, Q. Shao and X. Huang, *Chem. Soc. Rev.*, 2020, **49**, 3072–3106.
19 S. Kumari, R. Mitra, K. Biswas and A. Halder, *Int. J. Hydrogen Energy*, 2024, **80**, 1164–1173.
20 C. Yuan, H. B. Wu, Y. Xie and X. W. Lou, *Angew. Chem., Int. Ed.*, 2014, **53**, 1488–1504.
21 H. G. Edao, C. Y. Chang, W. B. Dilebo, F. T. Angerasa, E. A. Moges, Y. Nikodimos, C. B. Guta, K. Lakshmanan, J. L. Chen, M. C. Tsai, W. N. Su and B. J. Hwang, *ACS Appl. Mater. Interfaces*, 2024, **16**, 50602–50613.
22 J. Zhao, N. Liao and J. Luo, *J. Mater. Chem. A*, 2023, **11**, 9682–9690.
23 Z. Feng, E. Wang, S. Huang and J. Liu, *Nanoscale*, 2020, **12**, 4426–4434.
24 X. Tang, J. Y. Zhang, B. Mei, X. Zhang, Y. Liu, J. Wang and W. Li, *Chem. Eng. J.*, 2021, **404**, 126529.
25 J. Hou, X. Peng, J. Sun, S. Zhang, Q. Liu, X. Wang, J. Luo and X. Liu, *Inorg. Chem. Front.*, 2022, **9**, 3047–3058.
26 D. Raveendran, V. Mishra, A. E. Praveen, A. Roy, A. Basak, A. Chandrasekar and V. Mahalingam, *ChemCatChem*, 2025, **17**, e202401773.
27 V. Mishra, A. E. Praveen, D. Raveendran, A. Chandrasekar and V. Mahalingam, *Small*, 2025, **21**, 2412372.
28 A. Eftekhari, *Int. J. Hydrogen Energy*, 2017, **42**, 11053–11077.
29 Y. Li, Y. Zhao, F. M. Li, Z. Dang and P. Gao, *ACS Appl. Mater. Interfaces*, 2021, **13**, 34457–34467.
30 J. S. Samdani, J. Sanetuntikul and S. Shanmugam, *Int. J. Hydrogen Energy*, 2022, **47**, 27347–27357.
31 X. Peng, Y. Yan, X. Jin, C. Huang, W. Jin, B. Gao and P. K. Chu, *Nano Energy*, 2020, **78**, 105234.
32 Y. Li, X. Wei, L. Chen and J. Shi, *Angew. Chem., Int. Ed.*, 2021, **60**, 19550–19571.
33 C. B. Mendive, D. W. Bahnemann and M. A. Blesa, *Catal. Today*, 2005, **101**, 237–244.
34 Y. Gao and X. Peng, *J. Am. Chem. Soc.*, 2014, **136**, 6724–6732.
35 A. Heuer-Jungemann, N. Feliu, I. Bakaimi, M. Hamaly, A. Alkilany, I. Chakraborty, A. Masood, M. F. Casula, A. Kostopoulou, E. Oh, K. Susumu, M. H. Stewart, I. L. Medintz, E. Stratakis, W. J. Parak and A. G. Kanaras, *Chem. Rev.*, 2019, **119**, 4819–4880.
36 G. E. Ayom, M. D. Khan, F. M. de Souza, W. Lin, R. K. Gupta and N. Revaprasadu, *J. Energy Storage*, 2024, **97**, 112882.
37 A. E. Praveen, S. Ganguli, D. Sarkar and V. Mahalingam, *Inorg. Chem.*, 2022, **61**, 4394–4403.
38 S. Pradhan, R. Das, S. Biswas, D. K. Das, R. Bhar, R. Bandyopadhyay and P. Pramanik, *Electrochim. Acta*, 2017, **238**, 185–193.
39 B. Jiang, Y. Liu, J. Zhang, Y. Wang, X. Zhang, R. Zhang, L. L. Huang and D. Zhang, *RSC Adv.*, 2022, **12**, 1471–1478.
40 J. Singh, A. Gusain, V. Saxena, A. K. Chauhan, P. Veerender, S. P. Koiry, P. Jha, A. Jain, D. K. Aswal and S. K. Gupta, *J. Phys. Chem. C*, 2013, **117**, 21096–21104.
41 S. A. M. B. Dhas, M. Suresh, G. Bhagavannarayana and S. Natarajan, *J. Cryst. Growth*, 2007, **309**, 48–52.
42 M. Z. Fahmi, M. Wathoniyyah, M. Khasanah, Y. Rahardjo, S. Wafiroh and Abdulloh, *RSC Adv.*, 2018, **8**, 931–937.
43 X. Ma, J. Yang, X. Xu, H. Yang and C. Peng, *RSC Adv.*, 2021, **11**, 34432–34439.
44 D. Rakov, C. Sun, Z. Lu, S. Li and P. Xu, *Adv. Energy Sustainability Res.*, 2021, **2**, 2100071.
45 G. Wang, J. Chen, P. Cai, J. Jia and Z. Wen, *J. Mater. Chem. A*, 2018, **6**, 17763–17770.
46 J. Zhu and Y. Ni, *CrystEngComm*, 2018, **20**, 3344–3352.
47 X. Zheng, X. Han, H. Liu, J. Chen, D. Fu, J. Wang, C. Zhong, Y. Deng and W. Hu, *ACS Appl. Mater. Interfaces*, 2018, **10**, 13675–13684.
48 C. Wei, S. Sun, D. Mandler, X. Wang, S. Z. Qiao and Z. J. Xu, *Chem. Soc. Rev.*, 2019, **48**, 2518–2534.
49 C. Wei, R. R. Rao, J. Peng, B. Huang, I. E. L. Stephens, M. Risch, Z. J. Xu and Y. Shao-Horn, *Adv. Mater.*, 2019, **31**, 1806296.
50 X. Wang, M. Yu and X. Feng, *eScience*, 2023, **3**, 100141.
51 V. Mishra, A. E Praveen, A. Mondal and V. Mahalingam, *ACS Appl. Energy Mater.*, 2023, **6**, 3977–3985.
52 T. Shinagawa, A. T. Garcia-Esparza and K. Takanabe, *Sci. Rep.*, 2015, **5**, 13801.